A Highly Robust Ionotronic Fiber with Unprecedented Mechanomodulation of Ionic Conduction

Mingyue Yao, Baohu Wu, Xunda Feng, Shengtong Sun, and Peiyi Wu**

Stretchable ionic conductors are appealing for tissue-like soft electronics, yet suffer from a tardy mechanoelectric response due to their poor modulation of ionic conduction arising from intrinsic homogeneous soft chain network. Here, a highly robust ionotronic fiber is designed by synergizing ionic liquid and liquid crystal elastomer with alternate rigid mesogen units and soft chain spacers, which shows an unprecedented strain-induced ionic conductivity boost (≈10^3 times enhanced as stretched to 2000% strain). Such a surprisingly high enhancement is attributed to the formation of microphase-separated low-tortuosity ion-conducting nanochannels guided by strain-induced emergence of aligned smectic mesophases, thus allowing for ultrafast ion transport that resembles the role of "swimming lanes." Intriguingly, the boosting conductivity even reverses Pouillet's Law-dictated resistance increase at certain strains, leading to unique waveform-discernible strain sensing. Moreover, the fiber retains thermal actuation properties with a maximum of 70% strain changes upon heating, and enables integrated self-perception and actuation. The findings offer a promising molecular engineering route to mechanically modulate the ion transport behavior of ionic conductors toward advanced ionotronic applications.

1. Introduction

Ionic transport occurs widely and minutely in living matter to help with maintaining normal physiological activities.[1] For instance, skins and nerve fibers steadily transmit ion-based electrical signals even as largely deformed to retain the functions of precise self-perception and innervated feedback.[2] Inspired by the ion-conducting nature of human tissues, ionic conductor-based stretchable ionotronics has gained tremendous interest as artificial skins, muscles, axons, as well as in stretchable energy storage devices and soft robotics.[3–6] Nevertheless, unlike human tissues with rather complex and hierarchical structures, most of currently reported artificial ionic conductors, involving hydrogels, organohydrogels, ionogels, and ionic elastomers, were synthesized on the basis of a homogeneous solvent-swollen or salt-plasticized soft chain network.[4,7–11] Despite high stretchability and optical transparency, such a soft network shows negligible or very small modulating effect on ion transportation; as a result, the ionic conductivity does not change or only slightly increases as stretched due to the preferential orientation of elastic chains. Generally, the mechanoelectric response of the current ionic conductors is just between conductivity-constant conductors (e.g., ionic liquids,[12] liquid metals,[13] viscoelastic gels,[11] etc.; conductivity change, $\sigma/\sigma_0 = 1$) and resistance-constant conductors (e.g., buckling sheath-core fibers,[14] liquid metal-elastomer composites,[15] etc.; $\sigma/\sigma_0 = \lambda^2$, λ is the deformation ratio) (**Figure 1**a). It is well-known that the output resistance (R) is governed by Pouillet's Law ($R = L/(\sigma \cdot A)$), with A designating the cross-sectional area and L the length (during stretch, L increases while A is reduced). Understandably, the moderate electrical response of ionic conductors not only limits their strain sensing applications toward high gauge factors as do percolating electronic conductors with strain-induced deteriorated conductivity,[16] but also goes against interconnect applications that require strain-insensitive resistance to maintain stable electrical transmission. So far, it remains a formidable challenge for stretchable ionic conductors to overcome the seemingly inherent yet tardy mechanoelectric response arising from the poor modulating ability of soft chain network for ionic conduction.

It is reported that the network topology of ionic conductors at nanometer scales is of paramount importance in altering the mobility of ionic species.[17,18] In nanofluidics, tortuosity is defined as the ratio of actual ion pathway length to the straight end-to-end distance. Highly ordered or longitudinally aligned ion-insulating nanostructures can afford low-tortuosity pathways to promote ion transport and thus significantly reduce apparent resistance.[19] Therefore, it could be feasible to introduce large amounts of ion-insulating rigid molecular units into the elastic network of ionic conductors to modulate ion transport via tortuosity changes. We consider that, liquid crystal elastomers (LCEs) might be one of the best candidate materials for this purpose, as they encompass the properties of polymeric

M. Yao, X. Feng, S. Sun, P. Wu
State Key Laboratory for Modification of Chemical Fibers and Polymer Materials
College of Chemistry, Chemical Engineering and Biotechnology & Center for Advanced Low-dimension Materials
Donghua University
2999 North Renmin Road, Shanghai 201620, China
E-mail: shengtongsun@dhu.edu.cn; wupeiyi@dhu.edu.cn
B. Wu
Jülich Centre for Neutron Science (JCNS) at Heinz Maier-Leibnitz Zentrum (MLZ) Forschungszentrum Jülich
Lichtenbergstr. 1, 85748 Garching, Germany

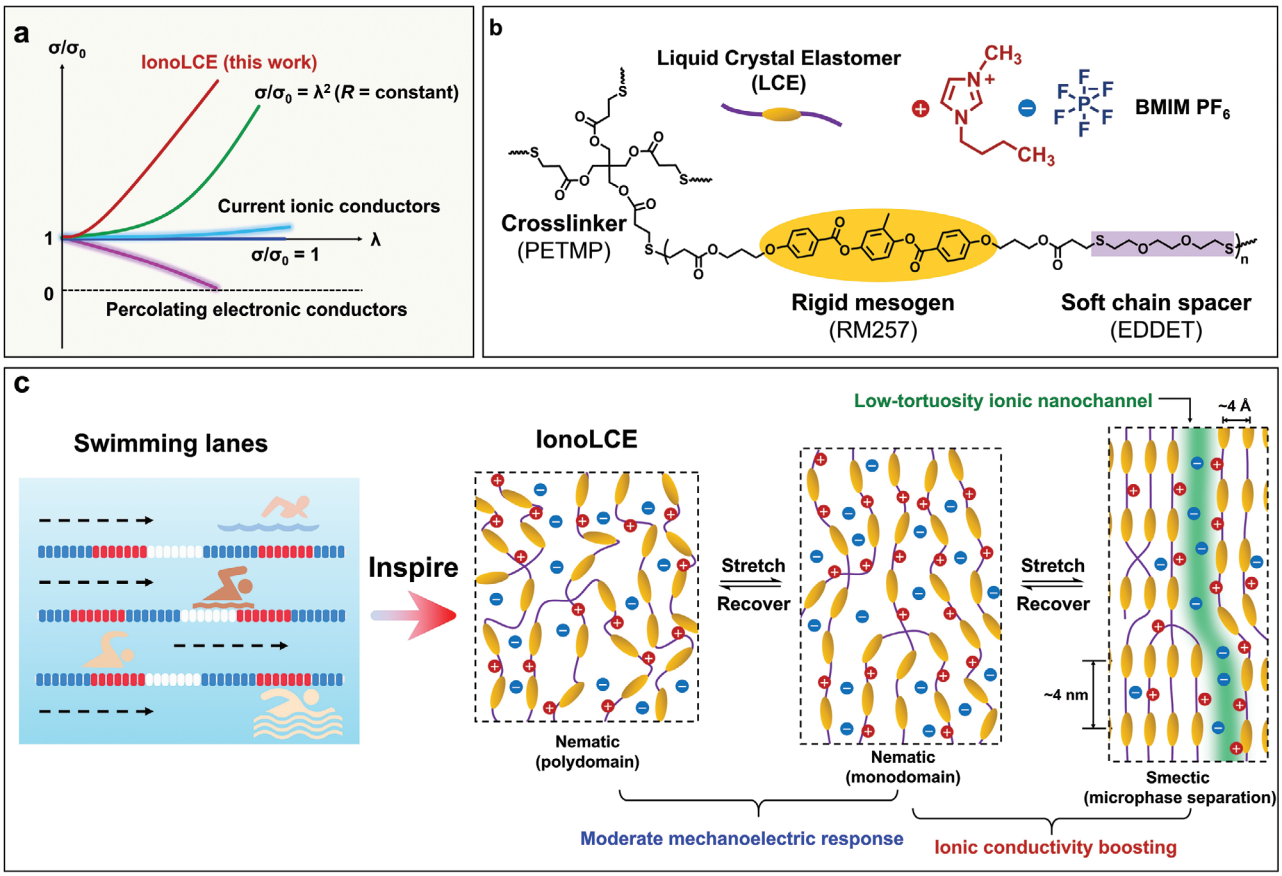

Figure 1. a) Mechanoelectric response of IonoLCE fiber in comparison with common electronic and ionic conductors. b) Molecular structures of IonoLCE consisting of ionic liquid (BMIM PF_6) and LCE network. c) Swimming lane-inspired working mechanism of IonoLCE. IonoLCE contains massive ion-insulating mesogens linked by BMIM-adsorbed soft chain spacers, and PF_6 anions are the main charge carriers. With stretch, IonoLCE experiences sequential transformations from nematic polydomain state to monodomain state (0–200% strain), and finally to microphase-separated smectic state featuring a longitudinal periodicity of ≈4 nm and shortened face-to-face mesogen distance of ≈4 Å. The former transition leads to only moderate mechanoelectric response, while the latter transition generates a number of interconnected low-tortuosity ionic nanochannels which result in promoted ion transport and significantly boosted ionic conductivity. Note that the whole process is fully reversible.

elastomers (entropy elasticity) with the self-organized assemblies of massive rigid mesogenic units.[20,21] The construction of interconnected ionic channels based on liquid crystals have been proved to function as efficient ion-conducting pathways.[22] Moreover, owing to its extraordinary reversible shape-changing properties in response to temperature, LCEs have been explored as excellent muscle-like actuating materials that have gained a variety of fascinating applications in soft robotics, sensors, and optics in recent years.[23–26]

Herein, for the first time, we demonstrate that by introducing ionic liquid (IL) into the LCE network to produce an ionotronic LCE (IonoLCE) fiber (see chemical structures in Figure 1b), low-tortuosity ion transport nanochannels would evolve via mesogen alignment-induced microphase separation during stretch, leading to the unprecedented strain-induced ionic conductivity boost (10^3 times enhancement at 2000% strain). Such a high enhancement factor has never been observed in any previously reported ionic conductors (σ/σ_0 is generally smaller than 5), and even surpasses the hotly studied resistance-constant electronic conductors (Figure 1a). Figure 1c depicts the working mechanism of the present IonoLCE fiber for ion transport modulation. As elucidated by our spectral and simulation analyses, IL mainly solvates the soft spacers of LCE via selective cation adsorption, yet rigid mesogens would force the anions to move only between them contributing to ionic conductivity. Prior to stretch, the fiber consists of slightly aligned polydomains of nematic mesophases while the ionic species are dispersed and nanoconfined in the network, leading to slow ion transport and low ionic conductivity. When the fiber is gradually stretched to the monodomain state (0–200% strain), mesogens become globally aligned, but at this state, the nanoconfinement of ions persists resulting in still a common moderate mechanoelectric response. However, as the fiber is further stretched (≥ 200% strain), an apparent nematic-to-smectic phase transition takes places along with microphase separation between LCE network and IL phase. The direct consequence is the formation of interconnected ion-conducting "highways" with low tortuosity and boosted ionic conductivity. Such an ion-conducting tortuosity effect is very similar to the case of "swimming lanes," in which swimmers always spend the shortest time to move from one end to another due to the lowest lane tortuosity. It is highlighted that

the very high conductivity enhancement factor even leads to the sharp resistance reduction of IonoLCE fiber at certain strains, which reverses the Pouillet's Law-dictated resistance increase. Therefore, as stretched to different strains, distinct waveforms of resistance changes can be recorded, which allows for unique signal shape-discernible sensing. Besides, IonoLCE fiber is rather robust showing high stretchability (≈2700% strain), excellent elastic recovery (99% recovered from 1200% strain), and ultrahigh toughness (56.9 MJ m^{-3}). More intriguingly, the thermal actuation properties of LCE are inherited by IonoLCE with even higher strain changes and work capacities. By incorporating a photothermal dye, we finally show that remote light-induced sensing and actuating can be simultaneously realized by the same IonoLCE fiber, demonstrating its great potential to be used in future advanced stretchable electronics.

2. Results and Discussion

IonoLCE fiber was prepared via the Michael addition reaction between acrylate-terminated reactive mesogen, RM257, and thiol-terminated chain spacer, 2,2′-(ethylenedioxy) diethanethiol (EDDET), in the presence of IL, BMIM PF_6 (see experimental details in the Supporting Information and reaction scheme in Figure S1). BMIM PF_6 was chosen as the ion-conducting solvent because the BMIM cation could selectively bind the soft spacer of LCE network via forming dynamic hydrogen bonds with ether groups, leaving PF_6 ions as the main charge carriers for conductivity control.[27,28] Pentaerythritol tetrakis(3-mercaptopropionate) (PETMP) was used as the cross-linker, and the precursor dissolved in 2-butanone was injected into a PTFE tube (inner diameter: 0.5 or 1 mm) for subsequent polymerization at room temperature. The ionotronic fiber was finally obtained by peeling from the tube followed by subsequent solvent evaporation. Note that we employed equimolar acrylate and thiol groups to completely consume all the monomers in one step, as supported by ATR-FTIR spectral comparison (Figure S2, Supporting Information). Using either excess RM257 or excess EDDET would lead to the largely deteriorated mechanical properties of the resulting fibers, probably due to the insufficient chain growth in the stepwise polymerization (Figure S3, Supporting Information). The content of IL was optimized to 30 wt% (weight ratio with respect to total monomers/cross-linker) to reach the maximum compatibility between IL and soft spacers (corresponding to ≈1:1 molar ratio of IL:EDDET), resulting in a fully transparent IonoLCE fiber (**Figure 2**a). A lower IL content than 30 wt% does not sufficiently plasticize the soft spacer of LCE, while further increasing IL contents would lead to apparent phase separations; the fibers produced in both of these two cases are opaque with less structural homogeneity and also reduced stretchability (see the photos, tensile curves, and scanning electron microscope (SEM) images of LCE/IL composite fibers with different IL contents in Figures S4–S6, Supporting Information).

It is interesting to find that the IonoLCE film prepared with the same recipe yet eliminated shear flow effect shows also high

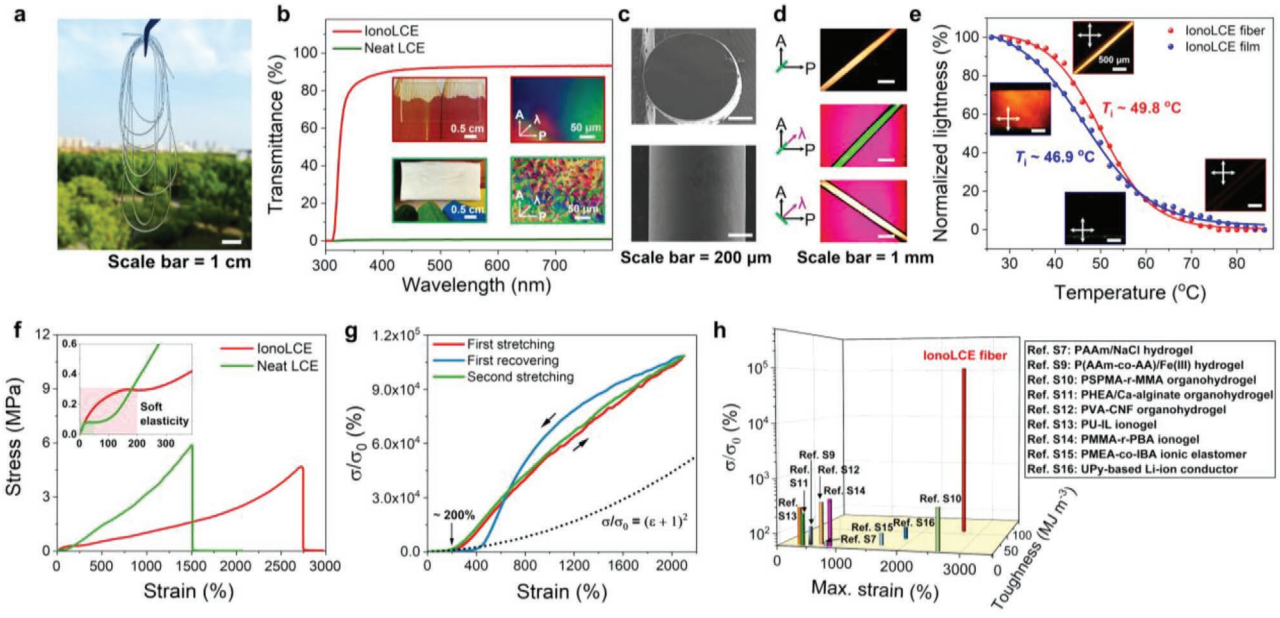

Figure 2. a) Photo of a transparent 1-m-long IonoLCE fiber. b) UV–vis spectra of IonoLCE and neat LCE films. The insets are corresponding photos and POM images. c) SEM images of the cross-section and outer surface of IonoLCE fiber. d) POM images of IonoLCE fiber. From top to bottom are the polarized modes in the absence of tint plate, and in the presence of 530 nm tint plate at azimuth angles of 45° and –45°, respectively. e) Normalized POM interference lightness changes of IonoLCE fiber and film as a function of temperature (insets: corresponding POM images at 28 and 86 °C, respectively). The transition temperatures were determined by Boltzmann fitting method. f) Tensile stress–strain curves of IonoLCE and neat LCE fibers. The inset is the zoom-in image at the small strains showing the initial "soft elasticity" regions (for IonoLCE fiber, 0–200% strain; for neat ICE, 0–50% strain). g) Strain-induced reversible ionic conductivity changes of IonoLCE fiber. The theoretical curve with constant resistance ($\sigma/\sigma_0 = \lambda^2 = (\varepsilon+1)^2$) is presented as a reference. The remarkable σ rise of IonoLCE fiber starts at ≈200% strain. h) Comparison of the maximum strain, toughness, and ionic conductivity enhancement (σ/σ_0 at 2000% strain) of IonoLCE fiber with other reported stretchable ionic conductors.

optical transparency of 92%, while neat LCE is totally opaque (Figure 2b). It is known that the opacity of neat LCE arises from the high-birefringence nematic polydomains that strongly scatter light.[29] Similar to neat LCE, transparent IonoLCE film shows also clear birefringence textures (insets in Figure 2b), indicating that IonoLCE at room temperature is in the polydomain state rather than isotropic state.[30] We ascribe the transparency of IonoLCE to the reduced birefringence difference due to the incorporation of IL in the LCE network, which is often observed in lytropic liquid crystals.[31] Moreover, the IonoLCE fiber shows a regular cylindrical shape with well-controlled round cross-section, as demonstrated by SEM observations (Figure 2c). We further employed polarized optical microscopy (POM) to examine the orientation and quality of the resultant IonoLCE fiber. As shown in Figure 2d, in the polarized mode, strong interference color of the fiber was observed, suggesting the presence of structural orientation. In the presence of a sensitive 530 nm tint plate, the sample showed green and orange interference colors at the azimuth angles of 45° and −45°, respectively. This can be ascribed to the unidirectional orientation of nematic domains parallel to the fiber direction. The fiber orientation may be induced by shear flow in the tube-injecting process, since the precursor solution had partially polymerized before injection.

By doping non-nematogenic IL species into LCE network, DSC detected the decrease of the glass transition temperature (T_g) of neat LCE from −3 to −10 °C, owing to the solvent-plasticizing effect (Figure S7, Supporting Information). Nevertheless, the typical nematic-to-isotropic phase transition completely disappears in IonoLCE fiber due to the weakened enthalpic change. To determine such a phase transition temperature, we monitored the relative lightness changes of the interference colors of IonoLCE fiber/film. As shown in Figure 2e, the Boltzmann fitted lightness changes of IonoLCE fiber and film show the nematic-to-isotropic transition temperatures (T_i) to be 49.8 and 46.9 °C, respectively. The higher transition temperature of IonoLCE fiber than film might be caused by the slight prealignment of polydomains as observed in POM observations. In addition, compared to neat LCE with a typical T_i at 79.9 °C, the reduced transition temperature of IonoLCE can be attributed to the so-called dilution effect of the nematic mean field ordering.[32]

As shown in Figure 2f, the IonoLCE fiber shows a maximum strain of 2700%, almost twice that of neat LCE (1500%). The Young's modulus, tensile strength, and toughness of the IonoLCE fiber are 0.5 MPa, 4.7 MPa, and 56.9 MJ m^{-3}, respectively, indicating its initial compliance (soft to touch) yet ultrahigh robustness to sustain large stresses and deformations. Such a robust feature was clearly demonstrated by easily lifting a 1.5 kg bottle water with a reversibly stretched IonoLCE fiber (Movie S1, Supporting Information). It is noted that the plasticizing effect of IL mainly occurs on the soft segment of LCE network, and thus the elongation is not too much improved yet the tensile strength remains high. With rubber elasticity theory, we further calculated the effective crosslinking densities of neat LCE and IonoLCE fibers to be 91.8 and 84.8 mol m^{-3}, respectively (see the calculation details in Supporting Information and Figure S8). Obviously, the presence of IL slightly decreases the crosslinking density of LCE network, which should also contribute to the increased elongation of IonoLCE fiber. In addition, both the IonoLCE and neat LCE fibers feature a "soft elasticity" region (i.e., strain softening response at low to moderate strains followed by strain-hardening at higher strains; for IonoLCE, the region is observed to be 0–200% strain, and for neat LCE, 0–50% strain). This unique viscoelastic mechanoresponse is characteristic for polydomain LCEs, which corresponds to the realignment of the mesogens in the polymer network to the stretch direction from local (polydomain) to global (monodomain) orientations.[33,34]

Intriguingly, as shown in Figure 2g, stretching the IonoLCE fiber caused the drastic increase of ionic conductivity after the soft elasticity region (calculated by the equation $\sigma/\sigma_0 = \lambda^2/(R/R_0)$; see details in Supporting Information), which is the direct evidence for the hypothesized low-tortuosity nanochannel-promoted fast ion transport. Similar strain-induced ionic conductivity boosting effect was also observed in the IonoLCE film, indicating that this phenomenon is independent of material shape and preparation method (Figure S9, Supporting Information). Moreover, such a process is fully reversible as evidenced from the recovering and second stretching ionic conductivity changes (Figure 2g). Microscopic observations did not detect the leakage of IL at even 2000% strain (Figure S10, Supporting Information), suggesting the strong binding capacity of LCE network on IL molecules that contributes to the excellent structural and conductive reversibility. Notably, the fiber shows an increase of ionic conductivity from 0.14 mS m^{-1} at 0% strain to 143.86 mS m^{-1} at 2000% strain, corresponding to more than 1000 times enhancement. Such a conductivity enhancement is even higher than the theoretical curve of resistance-constant conductors ($\sigma/\sigma_0 = \lambda^2$), which are critically important for stable electrical transmission as interconnects, but so far, were only reported in several electronically conducting systems.[14,35–37] Considering the ionic conductivity of IonoLCE fiber mainly arises from ion transportation, we also employed electrochemical impedance spectroscopy (EIS) to trace the charge-transfer resistance and corresponding ionic conductivity changes at certain strains.[10,38] The observed similar ionic conductivity boosting phenomenon after ≈200% strain further consolidates the hypothesis that it is indeed the promoted ion transportation that contributes to the enhanced ionic conductivity.

We here highlight that the combined mechanical properties and mechanoelectric response of IonoLCE fiber rank in the top level of current ionic conductors in terms of stretchability (maximum strain), toughness, and ionic conductivity enhancement (σ/σ_0), as demonstrated by the comparison plot with a few typical stretchable ionic conductors (Figure 2h and Table S1, Supporting Information).[7–9,39–44] Noteworthily, to the best of our knowledge, the strain-induced ionic conductivity enhancement factor of IonoLCE fiber (σ/σ_0 = 1028% at 2000% strain) is the reported highest value for neat ionic conductors; in sharp contrast, the conductivity change ratios of currently reported soft chain-based ionic conductors during stretch are generally smaller than 5.

The elasticity of IonoLCE fiber was further examined by cyclically stretching the fiber to the fixed strain of 1200% for 2000 cycles (**Figure 3**a), and the loading-unloading curves almost coincide after the first cycle (irreversible structures were

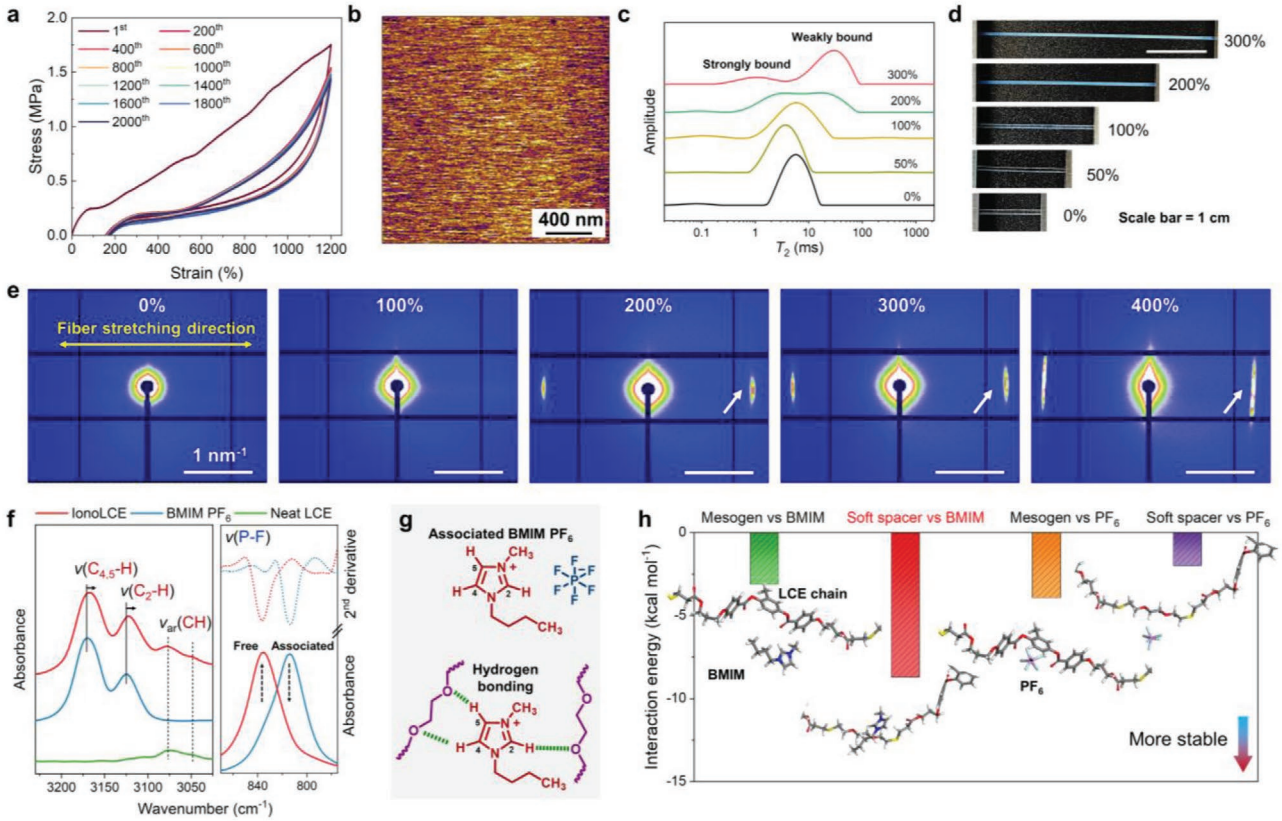

Figure 3. a) Cyclic stress–strain curves of IonoLCE fiber as stretched to 1200% strain for 2000 cycles (waiting time = 10 s). b) AFM height image of a spin-coated IonoLCE film. c) Low-field ^{19}F NMR spectra of IonoLCE fiber at different strains. d) Photos of IonoLCE fiber at different strains suggesting the evolution of microphase separation. e) 2D SAXS patterns of IonoLCE fiber at different strains. The arrows indicate the strong equatorial diffraction at $q = 1.57$ nm^{-1} corresponding to a smectic inter-layer distance of 4 nm. f) ATR-FTIR spectra of IonoLCE, BMIM PF$_6$ and neat LCE. Second-derivative spectra were shown for identifying the two components in PF$_6$ anions. g) Schematic main interactions in pure IL and IonoLCE. h) Interaction energies of the four pairs derived from molecular dynamics simulation. A lower energy value means that the conformation is thermodynamically more stable.

disrupted in the first cycle). The elastic recovery ratio calculated from the last cycles is ≈99%, suggesting the almost full recovery of IonoLCE fiber from large deformations in a short time. Cyclically stretching the fiber with increasing strains supports the same conclusion (Figure S12, Supporting Information). Moreover, a large hysteresis area is observed that can be directly related to the high toughness of IonoLCE fiber. As reported, the hysteresis represents an efficient energy-dissipation mechanism via sacrificial bonds,[45] which may be attributed to the dynamic hydrogen bonds between soft chain spacers and IL molecules in this material (will be discussed later).

To elucidate the internal structural changes hindered in the unprecedented phenomenon of strain-induced ionic conductivity enhancement, we first used atomic force microscope (AFM) to observe the microstructure of IonoLCE. As shown in Figure 3b, there is no apparent microphase separation in the as-prepared sample suggesting IonoLCE is indeed homogenous at the nanoscale. Low-field ^{19}F NMR was then utilized to monitor the molecular dynamics of PF$_6$ ions in IonoLCE fiber at different strains.[46] As shown in Figure 3c, there are two apparent changes of T_2 population. At 0–100% strain, there is only one peak which shifts to lower time domains first at 50% strain and then to higher time domains with a broader population at 100% strain. This may be because, in the low-strain soft elasticity region, the slight deformation of soft segments makes IL ions bind more closely due to the conformation adjustment of LCE network, and as further stretched, globally reoriented rigid mesogens are getting involved in promoting the movement of PF$_6$. At 200% strain, the unimodal peak splits into two peaks at lower and higher time domains, corresponding to strongly and weakly bound ILs, respectively. Further stretching the fiber to 300% strain intensifies the peak splitting event resulting in two peaks at even lower and higher time domains, and the amount of weakly bound PF$_6$ ions is also increased. As observed in Figure 3d, apparent phase separation has taken place at 200% strain along with the opacification of the fiber. The gradual opacity evolution of the fiber with stretch suggests that the phase-separated grains are continuously growing leading to enhanced light scattering . Therefore, it is understandable that the strain-induced alignment of mesogens in the monodomain state redistributes PF$_6$ ions into two categories with distinct mobilities: the strongly bound ones are still nanoconfined in the LCE network with low mobility, and the weakly bound ones are distributed in the phase-separated ionic nanochannels with higher mobility. Note that, although the weakly bound PF$_6$ ions in the ionic nanochannels are still not as mobile as in pure IL (T_2 ≈ 320 ms; Figure S13, Supporting Information), the nanochannel surface-governed nanofluidic ion transport effect[38]

strongly promotes the ionic conductivity of stretched IonoLCE fiber with only 30 wt% IL to approach the level of pure IL (σ = 144–150 mS m^{-1} at 25 °C) .[47]

Small-angle X-ray scattering (SAXS) method was further employed to study the microstructural changes during stretch. The 2D SAXS profile (Figure 3e) of the undeformed fiber appears as a slightly elongated circular halo at the small-angle region, resulting from the slightly aligned nematic polydomains in the whole fiber. Stretching the fiber to larger strains leads to the further elongation of the pattern into a date palm shape, ascribed to the gradual lengthening of the microstructural framework along stretching direction over a wide range of scales. Interestingly, at 200% strain, the SAXS pattern displays two strong equatorial diffraction spots at q = 1.57 nm^{-1}, corresponding to a real spacing of 4 nm. The sharp diffraction and the periodicity consist with the smectic layering of rigid mesogens with an inter-layer distance of 4 nm along the LC director that strictly follows the fiber direction. The consistence of the LC director with the layer normal as well as the absence of high-order diffraction in the SAXS pattern indicate that the generated LC phase is smectic-A.[48] Such a nematic-to-smectic transition is closely related to the observed microphase separation and the formation of low-tortuosity ion-conducting nanochannels, since the IL is excluded from the highly aligned and closely packed smectic domains. Further stretching does not significantly influence this layer periodicity (Figure S14, Supporting Information). Notably, at 400% strain, the equatorial diffraction spots in the SAXS pattern are elongated along the meridional direction, transforming into two narrow streaks. Such a transformation suggests that stretching induces the d-spacing decrease of smectic layers and the deviation of the smectic normal from the stretching direction (or the LC director). This geometry of the LC director tilted away from the layer normal implies the formation of smectic-C assemblies. The stretch-induced closer packing of the mesogens along with nematic-to-smectic transition is also supported by X-ray diffraction (XRD) comparison of IonoLCE at 0 and 400% strains. As shown in Figure S15, Supporting Information, aside the original peak at $2\theta = 20°$ corresponding to the nematic mean distance of 4.4 Å among mesogens, a new peak emerges at $2\theta = 22.3°$ that can be ascribed to the reduced face-to-face mesogen distance of 4.0 Å in the newly formed smectic phase.

Altogether, the above low-field ^{19}F NMR, SAXS, and XRD results primly support our hypothesis that the strain-induced ordered alignment of rigid mesogens in the LCE network can indeed induce the nematic-to-smectic transition and thus lead to the formation of phase-separated low-tortuosity ion-conducting pathways for promoted ion transportation. A turning point of ≈200% strain is found above which mesogens have assembled side by side with a shortened mean distance, resulting in excluding IL molecules from LCE network into the highly ordered ionic nanochannels. For comparison, the LCE/IL composite fibers containing higher IL contents than IonoLCE (30 wt%) with already occurred phase separations exhibit a largely reduced ionic conductivity boosting effect (Figure S16, Supporting Information), supporting the important role of an evolving microphase separation in the mechanomodulation of ionic conduction. In addition, along with the gradual structural adjustment in microphase separation, as demonstrated by the relaxation experiments (Figure S17, Supporting Information), the IonoLCE fiber takes ≈1 min to reach a relatively stable ionic conductivity when rapidly stretched to fixed large strains. Such a delayed conductivity response may account for the observed hysteresis of conductivity changes in Figure 2g.

We additionally performed ATR-FTIR spectral comparison to investigate the internal interactions in the IonoLCE fiber. Compared with pure IL, the C_2—H and $C_{4,5}$—H stretching vibrations of BMIM in IonoLCE both shift to lower wavenumbers (Figure 3f), suggesting the formation of multiple hydrogen bonds between BMIM and the ether group of soft spacers.[27,28] This is also supported by the higher amount of disordered C—O—C stretching in IonoLCE than in neat LCE due to the solvation effect of IL (Figure S18, Supporting Information). It is noted that the dynamic hydrogen bonds which may physically crosslink different soft segments serve as the important dissipation bonds to improve toughness, while the chemical crosslinks contribute to good elastic recovery. Meanwhile, the initially associated BMIM and PF_6 ion pairs are almost totally disrupted, inducing the significant peak shift of asymmetric P—F stretching at 814 cm^{-1} to a higher wavenumber (835 cm^{-1}) that is assigned to free PF_6 ions.[49] In other words, PF_6 anions are the main charge carriers in IonoLCE contributing to ionic conductivity. This also verifies the importance of low-field ^{19}F NMR findings that reflect the essential changes of ionic conduction. Moreover, the C—H stretching vibrations from the aromatic ring of rigid mesogens are not influenced by the addition of IL, suggesting that the mesogen group cannot be solvated by IL. However, C=O stretching of neat LCE slightly shifts to a higher wavenumber in IonoLCE, which can be explained by the less structural constraint of mesogens in the presence of IL (Figure S19, Supporting Information). The above conclusions were further confirmed by molecular dynamics simulation results. We constructed a model linear LCE chain with alternate rigid mesogen and soft spacer segments (Figure S20, Supporting Information), and then optimized the conformation when BMIM or PF_6 ion approached these two segments respectively. As shown in Figure 3h, the interaction energy between BMIM and soft spacer is the lowest among the four studied pairs, indicating the preferential adsorption of BMIM on the soft segments of LCE network.

We further demonstrate that the robust IonoLCE fiber could act as a durable and unique waveform-discernible strain sensor from the output resistance changes. Due to the remarkable strain-induced conductivity boost, the corresponding resistance change of IonoLCE fiber is totally different from the monotonous increasing trend as observed in other ionic conductors. As shown in **Figure 4**a, the conductivity boosting effect even reverses the Pouillet's Law-dictated shape-dependent resistance changes at certain strains. With stretch, the resistance changing rate ($\Delta R/R_0$) first increases to a maximum value of 178% at 121% strain (stage 1, gauge factor (GF) = 1.5), then decreases to a minimum of –79% at 618% strain (stage 2, GF = –1.2), and finally slightly increases at the following strains (stage 3, GF = 0.02). The initial resistance increasing trend generally follows the shape-correlated function, because at small strains, mesogens have not been globally aligned, and the deformation of LCE network with a weak mechanomodulation of ion conduction dominates electrical changes. Along with the

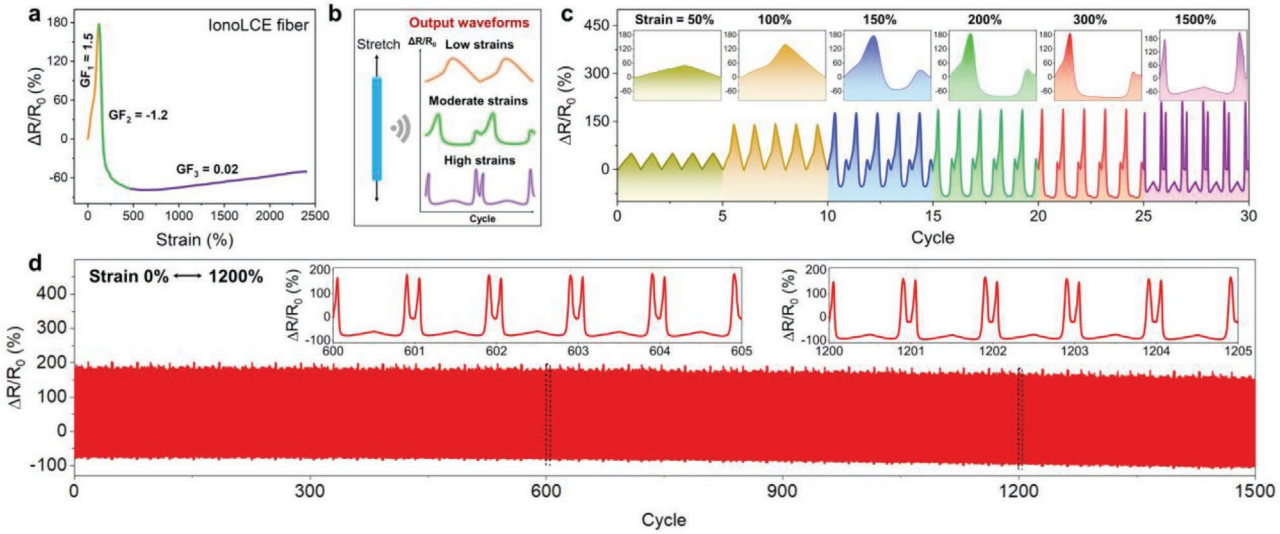

Figure 4. a) Strain-induced resistance changes of IonoLCE fiber. Corresponding gauge factors (GF = $\partial(\Delta R/R_0)/\partial\varepsilon$) at the three strain stages have been labeled. b) Schematic working mechanism of waveform-discernible strain sensing reported by IonoLCE fiber. c) Cyclically stretching the IonoLCE fiber to increasing strains produced repeatable electrical response with different waveforms. d) Real-time resistance changes of IonoLCE fiber by switching the strain between 0 and 1200% for 1500 cycles.

nematic-to-smectic transition and ionic conductivity boosting, an inversed resistance changing trend is observed from 121% to 618% strain. The abovementioned critical strain of 200% with the appearance of highly ordered ionic nanochannels corresponds to the point at which resistance decreases most rapidly. In the final stage, the conductivity boost cannot fully compensate the shape-correlated changes ($R/R_0 = \lambda^2/(\sigma/\sigma_0)$; λ^2 and σ/σ_0 both increase during stretch), and a slight resistance increase is thus observed.

Noteworthily, despite small and even negative gauge factors, the unique resistance changing curve of IonoLCE fiber allows for novel shape-discernible strain sensing applications. As demonstrated in Figure 4b,c, cyclically stretching the fiber to increasing strains produced well-resolved repeatable electrical signals with different waveforms (note that the releasing process has a hysteretic signal response compared with the stretching process). Such a unique performance will be very promising in reporting more diversified information about the deformation of sensors, while common ionic conductor-based strain sensors rely on only intensity variations.[7,9,12,50,51] Furthermore, the excellent elasticity and robustness of IonoLCE fiber render the sensor with outstanding durability. As shown in Figure 4d, stretching the fiber sensor to 1200% strain for 1500 cycles generated fully reproducible shape-featured electrical signals within a stable resistance level.

LCEs are known to be an excellent thermo-actuating material that mimics the functions of human muscles.[52] We here show that the incorporation of IL into LCE network does not sacrifice its intrinsic actuating properties. As subjected to a bias stress, heating the IonoLCE fiber from 35 to 85 °C generated sharp fiber contraction (**Figure 5**a). Upon the bias stress of 0.2 MPa, a maximum of ≈70% strain change was observed, suggesting a very high actuating performance. At the molecular level, the fiber at the bias stress-induced tension state with highly aligned mesogens would contract significantly through nematic/smectic-to-isotropic phase transition for entropy gain as the temperature is raised above a critical value (T_i = 49.8 °C for IonoLCE fiber).[23] As shown in Figure 5b, the actuation work capacity of IonoLCE fiber varies with the applied bias stress, and is much higher than neat LCE fiber (corresponding strain actuation curves in Figure S21, Supporting Information) in most cases. This is reasonable because the presence of IL largely increases the mobility of mesogens and thus promotes the conformation transition degree.[53] To render IonoLCE fiber with remote control ability over actuation, we further incorporated disperse red 1 (DR1), a photothermal dye with ultrafast cis-to-trans thermal relaxation absorbed at the visible region (Figure 5c),[54] into the IonoLCE network. Using a green laser (wavelength = 532 nm; power ≈ 50 mW) to scan along the fiber could quickly heat it to ≈95 °C, and the DR1-embedded IonoLCE fiber easily lifted a 20 g load as reflected by the synchronized normal and infrared thermal images (Figure 5d; Movie S2, Supporting Information). Similarly, the lifting action could also be observed by directly heating the fiber with a heat gun, which shares the same thermal actuation mechanism (Figure S22 and Movie S3, Supporting Information).

Furthermore, since the IonoLCE fiber is ionically conductive, integrated actuation and self-perception could be possible, which are fascinating for bioinspired smart actuating applications.[55] As an example in living systems, muscle spindles can actively sense the length changes of muscle which then convey the length information to central nervous system for guiding the muscle actuation as a feedback. In the case of IonoLCE fiber, temperature and strain both influence the output resistance signal. To simplify the demonstration, we fixed one DR1-embedded IonoLCE fiber between two clamps at a specified strain, and the photothermal-induced actuating stress and resistance changes can be simultaneously monitored with a force sensor and electrical multimeter, respectively (schematic set-up in Figure 5e). As shown in Figure 5f, the light-induced

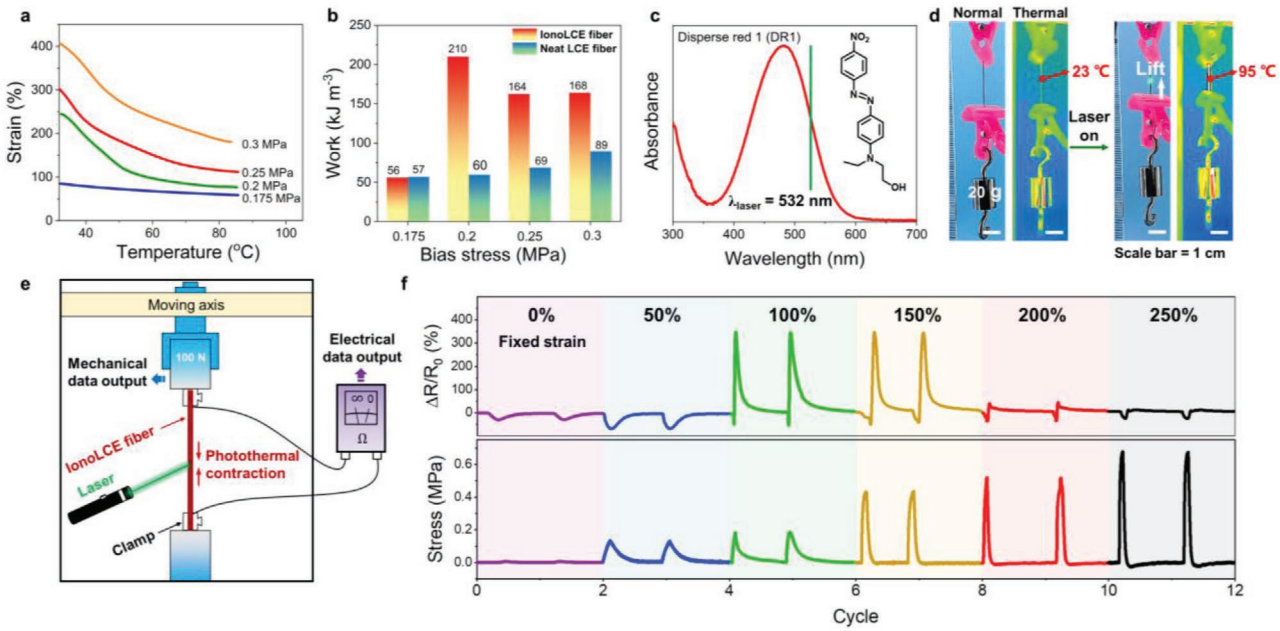

Figure 5. a) Thermal actuation-induced strain changes of IonoLCE fiber as subjected to different bias stresses. The strain of undeformed fiber at 30 °C is defined to 0%. b) Work capacities of IonoLCE and neat LCE fibers with increasing bias stresses. The work capacity was calculated by multiplying the bias stress by actuation strain (35–85 °C). c) UV–vis absorption spectrum and chemical structure of disperse red 1 (DR1). d) Upon 532 nm laser irradiation, the DR1-embedded IonoLCE fiber contracts to lift a 20 g load, as imaged by synchronized normal and infrared thermal cameras. e) Schematic set-up for simultaneously monitoring the actuating stress and electrical response of DR1-embedded IonoLCE fiber. f) Real-time stress and resistance pulsed changes of IonoLCE fiber upon irradiation with a green laser.

force pulses and corresponding electrical response could be well traced. With increasing fixed strains, the actuated stress becomes larger due to the more aligned mesogens that induce more remarkable thermal actuation. Nonetheless, the corresponding resistance changes show an unusual trend, which is presumed to result from the competing effect of temperature and mesogen alignment changes. That is, temperature increase always promotes ion mobility with the reduction of resistance. However, in IonoLCE fiber, heating also disturbs the ordered alignment of mesogens, leading to a lower ionic conductivity and thus resistance increment. At low fixed strains (0, 50%), the temperature effect is more predominant (R decrease), while at moderate fixed strains (100%, 150%), the mesogen alignment effect plays a dominating role (R first decrease and then increase). At even higher fixed strains (200%, 250%) with the occurrence of phase separation, the photothermal effect is unable to induce significant mesogen alignment changes due to the highly extended polymer chains in the smectic phase, and the temperature effect dominates again (R decrease with small amplitudes). Such an interesting competing effect not only proves the capability of IonoLCE fiber in real-time perceiving the actuating process, but also consolidates again the significance of mesogen alignment modulation in the mechanoelectric response of ionic conductors.

3. Conclusion

In summary, we report the first example of stretchable and highly robust ionically conducting fiber with surprisingly high strain-induced ionic conductivity enhancement through the mechanism of LCE-based mechanomodulation of ion transportation. The material design relies on the introduction of IL to selectively bind the soft chain spacer of LCE network, while the ion-insulating rigid mesogens serve as the important modulating units. Stretching leads to the formation of swimming lane-like low-tortuosity ionic nanochannels from the mesogen alignment-induced smectic phase separation. The resulting IonoLCE fiber shows high transparency (92%), high stretchability (2700% strain), good elastic recovery (99% from 1200% strain), high toughness (56.9 MJ m^{-3}), and most intriguingly, more than 10^3 times enhancement of ionic conductivity as stretched to 2000% strain. All these features render the fiber with unique waveform-discernible strain sensing advantages as well as integrated actuating and self-sensing functions. The present ionotronic actuating fiber and the clarified underlying conductivity-modulating mechanism not only highlight the fascination of structural design for regulating ion transport properties, but also open endless opportunities for developing mechanoresponsive ionic conductor-based miniaturized devices to be applied in next-generation stretchable electronics and soft robotics.

Supporting Information

Supporting Information is available from the Wiley Online Library or from the author.

Acknowledgements

The authors gratefully acknowledge the financial support from the National Science Foundation of China (NSFC) (Nos. 21991123, 51873035,

and 51733003) and Qimingxing Plan (No. 19QA1400200). The authors also thank the staffs from BL16B beamline at Shanghai Synchrotron Radiation Facility for assistance during data collection.

Conflict of Interest

The authors declare no conflict of interest.

Data Availability Statement

The data that support the findings of this study are available from the corresponding author upon reasonable request.

Keywords

actuators, ionic conductors, responsive materials, sensors, stretchable electronics

[1] Z. Zhu, D. Wang, Y. Tian, L. Jiang, *J. Am. Chem. Soc.* **2019**, *141*, 8658.
[2] M. Dong, B. Shi, D. Liu, J.-H. Liu, D. Zhao, Z.-H. Yu, X.-Q. Shen, J.-M. Gan, B.-l. Shi, Y. Qiu, C.-C. Wang, Z.-Z. Zhu, Q.-D. Shen, *ACS Nano* **2020**, *14*, 16565.
[3] C. Yang, Z. Suo, *Nat. Rev. Mater.* **2018**, *3*, 125.
[4] J.-Y. Sun, C. Keplinger, G. M. Whitesides, Z. Suo, *Adv. Mater.* **2014**, *26*, 7608.
[5] Y. Lee, W. J. Song, Y. Jung, H. Yoo, M.-Y. Kim, H.-Y. Kim, J.-Y. Sun, *Sci. Rob.* **2020**, *5*, eaaz5405.
[6] V. Vallem, Y. Sargolzaeiaval, M. Ozturk, Y.-C. Lai, M. D. Dickey, *Adv. Mater.* **2021**, *33*, 2004832.
[7] J. Song, S. Chen, L. Sun, Y. Guo, L. Zhang, S. Wang, H. Xuan, Q. Guan, Z. You, *Adv. Mater.* **2020**, *32*, 1906994.
[8] J. Lee, M. W. M. Tan, K. Parida, G. Thangavel, S. A. Park, T. Park, P. S. Lee, *Adv. Mater.* **2020**, *32*, 1906679.
[9] T. Li, Y. Wang, S. Li, X. Liu, J. Sun, *Adv. Mater.* **2020**, *32*, 2002706.
[10] L. Shi, T. Zhu, G. Gao, X. Zhang, W. Wei, W. Liu, S. Ding, *Nat. Commun.* **2018**, *9*, 2630.
[11] Z. Lei, P. Wu, *Nat. Commun.* **2019**, *10*, 3429.
[12] S. G. Yoon, H.-J. Koo, S. T. Chang, *ACS Appl. Mater. Interfaces* **2015**, *7*, 27562.
[13] Y. Qu, T. Nguyen-Dang, A. G. Page, W. Yan, T. D. Gupta, G. M. Rotaru, R. M. Rossi, V. D. Favrod, N. Bartolomei, F. Sorin, *Adv. Mater.* **2018**, *30*, 1707251.
[14] Z. F. Liu, S. Fang, F. A. Moura, J. N. Ding, N. Jiang, J. Di, M. Zhang, X. Lepro, D. S. Galvao, C. S. Haines, N. Y. Yuan, S. G. Yin, D. W. Lee, R. Wang, H. Y. Wang, W. Lv, C. Dong, R. C. Zhang, M. J. Chen, Q. Yin, Y. T. Chong, R. Zhang, X. Wang, M. D. Lima, R. Ovalle-Robles, D. Qian, H. Lu, R. H. Baughman, *Science* **2015**, *349*, 400.
[15] B. Yao, W. Hong, T. Chen, Z. Han, X. Xu, R. Hu, J. Hao, C. Li, H. Li, S. E. Perini, M. T. Lanagan, S. Zhang, Q. Wang, H. Wang, *Adv. Mater.* **2020**, *32*, 1907499.
[16] S. Choi, S. I. Han, D. Kim, T. Hyeon, D. H. Kim, *Chem. Soc. Rev.* **2019**, *48*, 1566.
[17] Y. Wang, Y. Chen, J. Gao, H. G. Yoon, L. Jin, M. Forsyth, T. J. Dingemans, L. A. Madsen, *Adv. Mater.* **2016**, *28*, 2571.
[18] Y. Wang, C. J. Zanelotti, X. Wang, R. Kerr, L. Jin, W. H. Kan, T. J. Dingemans, M. Forsyth, L. A. Madsen, *Nat. Mater.* **2021**, https://doi.org/10.1038/s41563-021-00995-4.
[19] Y. Shi, B. Li, Y. Zhang, Y. Cui, Z. Cao, Z. Du, J. Gu, K. Shen, S. Yang, *Adv. Energy Mater.* **2021**, *11*, 2003663.
[20] L. Yin, L. Han, F. Ge, X. Tong, W. Zhang, A. Soldera, Y. Zhao, *Angew. Chem., Int. Ed.* **2020**, *59*, 15129.
[21] H.-F. Lu, M. Wang, X.-M. Chen, B.-P. Lin, H. Yang, *J. Am. Chem. Soc.* **2019**, *141*, 14364.
[22] T. Kato, M. Yoshio, T. Ichikawa, B. Soberats, H. Ohno, M. Funahashi, *Nat. Rev. Mater.* **2017**, *2*, 17001.
[23] Z. Wang, K. Li, Q. He, S. Cai, *Adv. Mater.* **2019**, *31*, 1806849.
[24] Y. Zhang, Z. Wang, Y. Yang, Q. Chen, X. Qian, Y. Wu, H. Liang, Y. Xu, Y. Wei, Y. Ji, *Sci. Adv.* **2020**, *6*, eaay8606.
[25] A. S. Kuenstler, H. Kim, R. C. Hayward, *Adv. Mater.* **2019**, *31*, 1901216.
[26] Y. Wang, A. Dang, Z. Zhang, R. Yin, Y. Gao, L. Feng, S. Yang, *Adv. Mater.* **2020**, *32*, 2004270.
[27] D. F. Miranda, T. P. Russell, J. J. Watkins, *Macromolecules* **2010**, *43*, 10528.
[28] H.-C. Chang, T.-T. Tsai, M.-H. Kuo, *Macromolecules* **2014**, *47*, 3052.
[29] Z. Wang, W. Fan, Q. He, Y. Wang, X. Liang, S. Cai, *Extreme Mech. Lett.* **2017**, *11*, 42.
[30] C. M. Yakacki, M. Saed, D. P. Nair, T. Gong, S. M. Reed, C. N. Bowman, *RSC Adv.* **2015**, *5*, 18997.
[31] X. Feng, Q. Imran, Y. Zhang, L. Sixdenier, X. Lu, G. Kaufman, U. Gabinet, K. Kawabata, M. Elimelech, C. O. Osuji, *Sci. Adv.* **2019**, *5*, eaav9308.
[32] L. A. Serrano, M. J. Fornerod, Y. Yang, S. Gaisford, F. Stellacci, S. Guldin, *Soft Matter* **2018**, *14*, 4615.
[33] B. R. Donovan, H. E. Fowler, V. M. Matavulj, T. J. White, *Angew. Chem., Int. Ed.* **2019**, *58*, 13744.
[34] J. Schätzle, W. Kaufhold, H. Finkelmann, *Makromol. Chem.* **1989**, *190*, 3269.
[35] F. Sun, M. Tian, X. Sun, T. Xu, X. Liu, S. Zhu, X. Zhang, L. Qu, *Nano Lett.* **2019**, *19*, 6592.
[36] Z. Ma, Q. Huang, Q. Xu, Q. Zhuang, X. Zhao, Y. Yang, H. Qiu, Z. Yang, C. Wang, Y. Chai, Z. Zheng, *Nat. Mater.* **2021**, *20*, 859.
[37] S. Liu, D. S. Shah, R. Kramer-Bottiglio, *Nat. Mater.* **2021**, *20*, 851.
[38] H. Park, K. H. Lee, Y. B. Kim, S. B. Ambade, S. H. Noh, W. Eom, J. Y. Hwang, W. J. Lee, J. Huang, T. H. Han, *Sci. Adv.* **2018**, *4*, eaau2104.
[39] C. Keplinger, J.-Y. Sun, C. C. Foo, P. Rothemund, G. M. Whitesides, Z. Suo, *Science* **2013**, *341*, 984.
[40] H. Lei, L. Dong, Y. Li, J. Zhang, H. Chen, J. Wu, Y. Zhang, Q. Fan, B. Xue, M. Qin, B. Chen, Y. Cao, W. Wang, *Nat. Commun.* **2020**, *11*, 4032.
[41] B. Yiming, Y. Han, Z. Han, X. Zhang, Y. Li, W. Lian, M. Zhang, J. Yin, T. Sun, Z. Wu, T. Li, J. Fu, Z. Jia, S. Qu, *Adv. Mater.* **2021**, *33*, 2006111.
[42] Y. Ye, Y. Zhang, Y. Chen, X. Han, F. Jiang, *Adv. Funct. Mater.* **2020**, *30*, 2003430.
[43] M. Ju, B. Wu, S. Sun, P. Wu, *Adv. Funct. Mater.* **2020**, *30*, 1910387.
[44] Y. M. Kim, H. C. Moon, *Adv. Funct. Mater.* **2020**, *30*, 2070020.
[45] M. Hua, S. Wu, Y. Ma, Y. Zhao, Z. Chen, I. Frenkel, J. Strzalka, H. Zhou, X. Zhu, X. He, *Nature* **2021**, *590*, 594.
[46] W.-H. Zhang, M.-J. Yin, Q. Zhao, C.-G. Jin, N. Wang, S. Ji, C. L. Ritt, M. Elimelech, Q.-F. An, *Nat. Nanotechnol.* **2021**, *16*, 337.
[47] M. Kanakubo, K. R. Harris, N. Tsuchihashi, K. Ibuki, M. Ueno, *J. Phys. Chem. B* **2007**, *111*, 2062.
[48] J. Stamatoff, P. E. Cladis, D. Guillon, M. C. Cross, T. Bilash, P. Finn, *Phys. Rev. Lett.* **1980**, *44*, 1509.
[49] T. Buffeteau, J. Grondin, J.-C. Lassègues, *Appl. Spectrosc.* **2010**, *64*, 112.
[50] W. Zhang, B. Wu, S. Sun, P. Wu, *Nat. Commun.* **2021**, *12*, 4082.

[51] C. He, S. Sun, P. Wu, *Mater. Horiz.* **2021**, *8*, 2088.
[52] C. Zhu, Y. Lu, L. Jiang, Y. Yu, *Adv. Funct. Mater.* **2021**, *31*, 2009835.
[53] M. O. Saed, A. H. Torbati, C. A. Starr, R. Visvanathan, N. A. Clark, C. M. Yakacki, *J. Polym. Sci., Part B: Polym. Phys.* **2017**, *55*, 157.
[54] A. H. Gelebart, D. J. Mulder, M. Varga, A. Konya, G. Vantomme, E. W. Meijer, R. L. B. Selinger, D. J. Broer, *Nature* **2017**, *546*, 632.
[55] X.-Q. Wang, K. H. Chan, Y. Cheng, T. Ding, T. Li, S. Achavananthadith, S. Ahmet, J. S. Ho, G. W. Ho, *Adv. Mater.* **2020**, *32*, 2000351.